Inorg. Chem. **2008**, *47*, 5079−5092

Dicobalt II−II, II−III, and III−III Complexes as Spectroscopic Models for Dicobalt Enzyme Active Sites

Frank B. Johansson,[†] Andrew D. Bond,[†] Ulla Gro Nielsen,[†] Boujemaa Moubaraki,[‡] Keith S. Murray,[‡] Kevin J. Berry,[§] James A. Larrabee,*[,||] and Christine J. McKenzie*[,†]

Department of Physics and Chemistry, University of Southern Denmark, Campusvej 55, 5230 Odense M, Denmark, School of Chemistry, Building 23, Monash University, Clayton, Victoria Australia, Department of Chemistry and Biochemistry, Middlebury College, Middlebury, Vermont, U.S.A., and Westernport Secondary College, Hastings, Victoria, 3915, Australia

Received October 17, 2007

A matched set of dinuclear cobalt complexes with II−II, II−III, and III−III oxidation states have been prepared and structurally characterized. In $[(bpbp)Co_2(O_2P(OPh)_2)_2]^{n+}$ ($n = 1$, 2, or 3; $bpbp^- = 2,6$-bis((*N,N*′-bis-(2-picolyl)amino)-methyl)-4-tertbutylphenolato), the nonbonded Co···Co separations are within the range 3.5906(17) to 3.7081(11) Å, and the metal ions are triply bridged by the phenolate oxygen atom of the heptadentate dinucleating ligand and by two diphenylphosphate groups. The overall structures and geometries of the complexes are very similar, with minor variations in metal−ligand bond distances consistent with oxidation state assignments. The $Co^{II}Co^{III}$ compound is a valence-trapped Robin−Day class II complex. Solid state ^{31}P NMR spectra of the diamagnetic $Co^{III}Co^{III}$ (**3**) and paramagnetic $Co^{II}Co^{III}$ (**2**) and $Co^{II}Co^{II}$ (**1**) complexes show that ^{31}P isotropic shifts broaden and move downfield by about 3000 ppm for each increment in oxidation state. Cyclic voltammetry corroborates the existence of the $Co^{II}Co^{II}$, $Co^{II}Co^{III}$, and $Co^{III}Co^{III}$ species in solution. The redox changes are not reversible in the applied scanning timescales, indicating that chemical changes are associated with oxidation and reduction of the cobalt centers. An investigation of the spectroscopic properties of this series has been carried out for its potential usefulness in analyses of the related spectroscopic properties of the dicobalt metallohydrolases. Principally, magnetic circular dichroism (MCD) has been used to determine the strength of the magnetic exchange coupling in the $Co^{II}Co^{II}$ complex by analysis of the variable-temperature variable-field (VTVH) intensity behavior of the MCD signal. The series is ideal for the spectroscopic determination of magnetic coupling since it can occur only in the $Co^{II}Co^{II}$ complex. The $Co^{II}Co^{III}$ complex contains a nearly isostructural Co^{II} ion, but since Co^{III} is diamagnetic, the magnetic coupling is switched off, while the spectral features of the Co^{II} ion remain. Analysis of the MCD data from the $Co^{II}Co^{III}$ complex has been undertaken in the theoretical context of a $^4T_{1g}$ ground-state of the Co^{II} ion, initially in an octahedral ligand field that is split by both geometric distortion and zero-field splitting to form an isolated doublet ground state. The MCD data for the $Co^{II}Co^{II}$ pair in the $[(bpbp)Co_2(O_2P(OPh)_2)_2]^+$ complex were fitted to a model based on weak antiferromagnetic coupling with $J = -1.6$ cm^{-1}. The interpretation is confirmed by solid state magnetic susceptibility measurements.

Introduction

An understanding of the electronic properties of dinuclear Co^{II} complexes will provide insight into the electronic interactions and reactivity of dinuclear Co^{II} active sites in proteins. Methionine aminopeptidase (MetAP) is an ubiquitous dinuclear metallohydrolase responsible for removal of the *N*-terminal methionine in nascent proteins. Extensive studies have been conducted on the dicobalt form of the enzyme, and structural determinations of human,[1] *Pyrococcus furiousus*,[2] and *Escherichia coli*[3a] MetAPs have revealed

* To whom correspondence should be addressed. E-mail: larrabee@middlebury.edu (J.A.L.), chk@ifk.sdu.dk (C.J.M.).
[†] University of Southern Denmark.
[‡] Monash University.
[§] Westernport Secondary College.
[||] Middlebury College.

(1) Roderick, S. L.; Matthews, B. W. *Biochemistry* **1993**, *32*, 3907–3912.

10.1021/ic7020534 CCC: $40.75
Published on Web 05/22/2008

Scheme 1. Schematic Diagrams of Four Dicobalt Active Sites (Distances Shown in Å)

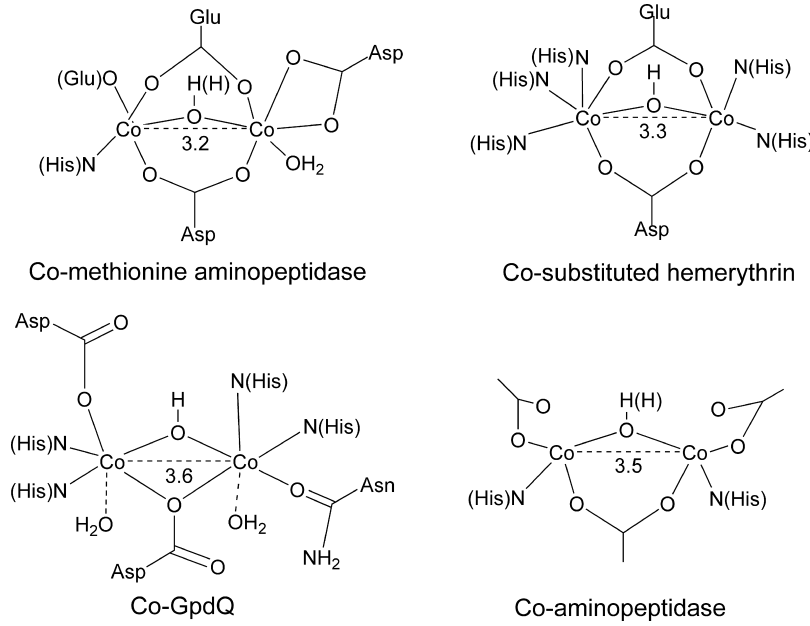

structurally similar dicobalt centers in the active sites. They consist of two metal ions bridged by a hydroxide ion (or a water molecule), one aspartate, and one glutamate. A recent structure determination of MetAP from *E. coli* found one of the Co^{II} ions to be hexacoordinated in a distorted octahedral environment, having a coordinated water and bidentate aspartate completing its coordination sphere. The second Co^{II} ion is pentacoordinated in a distorted trigonal-bipyramidal arrangement, with an imidazole nitrogen from histidine and a monodentate glutamate completing the pentacoordination. The carboxylate-bridged dimetallic active site is a common structural motif in proteins and enzymes (Scheme 1). Other proteins in this category include aminopeptidase, the dioxygen carrier protein, hemerythrin, several phosphatases, and phosphoesterases, such as glycerophosphodiesterase from *Enterobacter aerogenes* (GpdQ).[3] Few of these enzymes have cobalt as the in vivo metal, but most are fully active or even hyperactive in the dicobalt form. For example, MetAP is likely a Mn^{II} enzyme, but most of the structural and biochemical studies to date have been conducted on the Co^{II} form.[3e,f] Often the cobalt forms of these proteins are studied because Co^{II} is an excellent spectroscopic probe.

One key parameter for comparing dinuclear Co^{II} complexes is the strength of the magnetic exchange coupling. This is usually reported as "*J*" when using the isotropic Heisenberg−Dirac−van Vleck (HDVV) theoretical model. *J* is defined throughout this paper and in Table 7 by use of the Hamiltonian $-2J\mathbf{S_1}.\mathbf{S_2}$. Many of the papers cited herein use $-J\mathbf{S_1}.\mathbf{S_2}$ and thus their quoted *J* is equal to our 2*J*. In MetAP it has been demonstrated that some inhibitors and substrate analogs displace or interact with the bridging hydroxide. In such situations, perturbation of the magnetic coupling is expected.[2] It has been demonstrated that the diiron active site in pig purple acid phosphatase is weakly antiferromagnetically coupled at low pH while the mixed iron/manganese active site in a sweet potato purple acid phosphatase is strongly coupled at the same pH.[3c] This has been interpreted in terms of the presence of a μ-hydroxo bridge in the diiron enzyme and a μ-oxo bridge in the mixed-metal enzyme. The study of model systems will aid understanding of the structural parameters that influence the magnitude and sign of magnetic coupling so that measurements in enzyme active sites can be interpreted. However, there is currently a paucity of reported magnetic coupling strengths for dinuclear Co^{II} complexes that are structurally similar to MetAP and related enzymes, partly because of the experimental and theoretical difficulty in the quantitative determination of magnetic coupling strength in high-spin Co^{II} dimers, and partly for the lack of suitable complexes. Some dinuclear phosphate-bridged $Co^{II}Co^{III}$ complexes have been structurally characterized, but these have been used predominantly to investigate phosphate hydrolysis.[4] Brown et

(2) (a) Lowther, W. T.; Orville, A. M.; Madden, D. T.; Lim, S.; Rich, D. H.; Matthews, B. W. *Biochemistry* **1999**, *38*, 7678–7688. (b) Lowther, W. T.; Zhang, Y.; Sampson, P. B.; Honek, J. F.; Matthews, B. W. *Biochemistry* **1999**, *38*, 14810–14819.

(3) (a) Lowther, W. T.; Matthews, B. W. *Chem. Rev.* **2002**, *102*, 4581–4608. (b) Wilcox, D. E. *Chem. Rev.* **1996**, *96*, 2435–2458. (c) Mitic, N.; Smith, S. J.; Neves, A.; Guddat, L. W.; Gahan, L. R.; Schenk, G. *Chem. Rev.* **2006**, *106*, 3338–3363. (d) Jackson, C. J.; Carr, P. D.; Liu, J-W.; Watt, S. J.; Beck, J. L.; Ollis, D. L. *J. Mol. Biol.* **2007**, *367*, 1047–1062. (e) Wang, J.; Sheppard, G. S.; Lou, P.; Kawai, M.; Park, C.; Egan, D. A.; Schneider, A.; Bouska, J.; Lesniewski, R.; Henkin, J. *Biochemistry* **2003**, *42*, 5035–5042. (f) Copik, A. J.; Nocek, B. P.; Swierczek, S. I.; Ruebush, S.; Jang, S. B.; Meng, L.; D'sousa, V. M.; Peters, J. W.; Bennett, B.; Holz, R. C. *Biochemistry* **2005**, *44*, 121–129.

(4) (a) Wahnon, D.; Lebuis, A.-M.; Chin, J. *Angew. Chem., Int. Ed. Engl.* **1995**, *34*, 2412–2414. (b) Seo, J. S.; Sung, N.-D.; Hynes, R. C.; Chin, J. *Inorg. Chem.* **1996**, *35*, 7472–7473. (c) Seo, J. S.; Hynes, R. C.; Williams, D.; Chin, J. *J. Am. Chem. Soc.* **1998**, *120*, 9943–9944. (d) Williams, N. H.; Cheung, W.; Chin, J. *J. Am. Chem. Soc.* **1998**, *120*, 8079–8087.

al.,[5] Ostrovsky et al.,[6a,b] Ye et al.[7] and Sakiyama et al.[8d] have prepared and characterized several dinuclear Co^{II} complexes having acetate bridging ligands, and in some cases, an additional bridging oxygen atom from another ligand. The reported coupling constants for these complexes are all in the range of weak antiferromagnetic coupling ($J = -0.2$ to -6.9 cm^{-1}), except for one complex reported to exhibit moderate ferromagnetic coupling ($J = 18.0$ cm^{-1}) resulting in a μ_{eff} versus temperature plot that had a broad maximum at ~100 K.[6b] In some of these reports the Hamiltonian used in the HDVV model neglected zero-field splitting, which can affect the magnitude of *J*. Orbital contributions, which can be important for highly symmetric Co^{II} dimers, have been considered in a number of complexes after it was shown that the HDVV coupling model was inadequate because of strong spin−orbit coupling and ligand-field octahedral distortion effects.[6b,8a,c,d]

We have used magnetic circular dichroism (MCD) to probe the magnetic coupling in the $Co^{II}Co^{II}$ complex through analysis of the temperature dependence of the MCD signal. The $Co^{II}Co^{III}$ and $Co^{II}Co^{II}$ complexes described herein are ideally suited to test this spectroscopic method. In such systems, properties in the ground-state that are due to coupling can be isolated from those due to the uncoupled Co^{II} "monomeric" ground state. Such systems for cobalt have been known for some time. For example, Wieghardt et al. have reported a series of complexes having a $Co_2(\mu\text{-}X)(\mu\text{-}OAc)_2^{n+}$ (X = OH, Cl, or Br; $n = 1-3$) core, for which the $Co^{II}Co^{II}$, $Co^{II}Co^{III}$, and $Co^{III}Co^{III}$ combinations were prepared.[9] However, quantitative magnetic properties were not reported for that series. We report here an investigation of the structural, spectroscopic, electrochemical, and electronic properties of a matched set of related dinuclear $Co^{II}Co^{II}$, $Co^{II}Co^{III}$, and $Co^{III}Co^{III}$ complexes in which the donor set to each metal ion is identical and the metal ions are bridged by two diphenyl phosphate bridging groups and a bridging phenolate oxygen atom. With respect to the analogy to dicobalt enzyme active sites, the phosphate bridging groups resemble the bridging carboxylate groups in MetAP and a proposed intermediate in the purple acid phosphatase mechanism.[3] The series is ideal for the spectroscopic probing of magnetic coupling since magnetic coupling can occur only in the $Co^{II}Co^{II}$ complex. The $Co^{II}Co^{III}$ complex contains a nearly isostructural Co^{II} ion, but since Co^{III} is diamagnetic, the magnetic coupling is switched off, while the spectral features of the Co^{II} ion remain.

MCD has proved to be a generally useful probe of the ground-state electronic properties of paramagnetic metal ions in protein active sites,[10] and the technique has been used previously to examine some coupled diiron species.[11] MCD has distinct advantages over other techniques such as temperature-dependent magnetic susceptibility and electron paramagnetic resonance spectroscopy. In particular, MCD is not a bulk property technique like magnetic susceptibility, so it is not prone to errors introduced by paramagnetic impurities that are likely in protein preparations. MCD is particularly sensitive to transition metals having unpaired electrons, so it is well-suited to study metalloenzymes that are by nature magnetically dilute. In addition, MCD can be used to examine a specific metal ion, even in mixed-metal or mixed-valent systems. The present study serves as a first demonstration of the application of MCD to measure weak antiferromagnetic coupling in a dinuclear Co complex in which the coupling can be turned "on" or "off".

Results and Discussion

Synthesis. The $Co^{II}Co^{II}$ complex $[(bpbp)Co_2(O_2P(OPh)_2)_2](ClO_4)\cdot H_2O$, **1**-$(ClO_4)\cdot H_2O$, is obtained from stoichiometric reaction of the protonated ligand bpbpH, cobalt perchlorate, and diphenylphosphonic acid in acetonitrile. We note that under the same aerobic conditions with diphenylphosphonic acid replaced by acetic acid, the product is a dicobalt(III) acetate and peroxide-bridged complex, rather than the *bis*-oxoacid bridged complex $[(bpbp)Co_2(CH_3CO_2)_2]^+$.[12] The change of auxiliary bridge (RO_2^-) from $CH_3CO_2^-$ to $(C_6H_5O)_2PO_2^-$ clearly diminishes the propensity for the $[Co^{II}_2(bpbp)(RO_2)]^{2+}$ core to react with O_2, consequently Co^{II} complexes are relatively stabilized. The mixed-valence $Co^{II}Co^{III}$ complex, $[(bpbp)Co_2(O_2P(OPh)_2)_2](ClO_4)_2\cdot C_3H_6O\cdot H_2O$, **2**-$(ClO_4)_2\cdot C_3H_6O\cdot H_2O$, and the $Co^{III}Co^{III}$ complex $[(bpbp)Co_2(O_2P(OPh)_2)_2](ClO_4)_3\cdot 3.5H_2O$, **3**-$(ClO_4)_3\cdot 3.5H_2O$, were obtained, quite controllably, by reacting **1** with one equivalent of Ce^{IV} and ten equivalents of Ce^{IV}, respectively. The ^{13}C and ^1H NMR of **3** give sharp signals, as expected of a diamagnetic complex. Only five nonaromatic

(5) (a) Brown, D. A.; Errington, W.; Glass, W. K.; Haase, W.; Kemp, T. J.; Nimir, H.; Ostrovsky, S. M.; Werner, R. *Inorg. Chem.* **2001**, *40*, 5962–5971. (b) Brown, D. A.; Glass, W. K.; Fitzpatrick, N. J.; Kemp, T. J.; Errington, W.; Clarkson, G. J.; Haase, W.; Karsten, F.; Mahdy, A. H. *Inorg. Chim. Acta* **2004**, *357*, 1411–1436. (c) Brown, D. A.; Glass, W. K.; Fitzpatrick, N. J.; Kemp, T. J.; Errington, W.; Muller-Bunz, H.; Hussein, A. J.; Nimir, H. *Inorg. Chim. Acta* **2005**, *358*, 2755–2762.

(6) (a) Ostrovsky, S. M.; Werner, R.; Brown, D. A.; Haase, W. *Chem. Phys. Lett.* **2002**, *353*, 290–294. (b) Ostrovsky, S. M.; Falk, K.; Pelikan, J.; Brown, D. A.; Tomkowicz, Z.; Haase, W. *Inorg. Chem.* **2006**, *45*, 688–694. (c) Turpeinen, U.; Ahlgren, M.; Hamalainen, R. *Acta Crystallogr.* **1982**, *B38*, 1580–1583.

(7) (a) Schultz, B. E.; Ye, B.-H.; Li, X.-Y.; Chan, S. I. *Inorg. Chem.* **1997**, *36*, 2617–2622. (b) Ye, B.-H.; Chen, X. M. *Chin. J. Chem.* **2003**, *21*, 531–536. (c) Ye, B.-H.; Williams, I. D.; Li, X.-Y. *J. Inorg. Biochem.* **2002**, *92*, 128–136.

(8) (a) Fink, K.; Wang, C.; Staemmler, V. *Inorg. Chem.* **1999**, *38*, 3847–3856. (b) Tsukerblat, B. S.; Palii, A. V.; Turta, K.; Jovmir, T.; Shova, S.; Bartolome, J.; Evangelisti, M.; Filoti, G. *J. Chem. Phys.* **2001**, *115*, 9528–9535. (c) Hossain, M. J.; Yamasaki, M.; Mikuriya, M.; Kuribayashi, A.; Sakiyama, H. *Inorg. Chem.* **2002**, *41*, 4058–4062. (d) Sakiyama, H. *Inorg. Chim. Acta* **2006**, *359*, 2097–2100. (e) Aromi, G.; Stoeckli-Evans, H.; Teat, S. J.; Cano, J.; Ribas, J. *J. Mater. Chem.* **2006**, *16*, 2635–2644.

(9) Chaudhuri, P.; Querbach, J.; Wieghardt, K.; Nuber, B.; Weiss, J. *J. Chem. Soc., Dalton Trans.* **1990**, 271–278.

(10) (a) Johnson, M. K. In *Physical Methods in Bioinorganic Chemistry*; Que, L., Jr., Ed.; University Science Books: Sausilito, CA, 2000; Chapter 5. (b) Pavel, E. G.; Solomon, E. I. In *Spectroscopic Methods in Bioinorganic Chemistry*; Solomon, E. I., Hodgson, K. O., Eds.; American Chemical Society: Washington, DC, 1998; Chapter 6. (c) Wei, P.; Tomter, A. B.; Rohr, A. K.; Andersson, K. K.; Solomon, E. I. *Biochemistry* **2006**, *45*, 14043–14051.

(11) (a) Reem, R. C.; Solomon, E. I. *J. Am. Chem. Soc.* **1987**, *109*, 1216–1226. (b) Pulver, S. C.; Tong, W. H.; Bollinger, J. M.; Stubbe, J.; Solomon, E. I. *J. Am. Chem. Soc.* **1995**, *117*, 12664–12678. (c) Wei, P.; Skulan, A. J.; Mitic, N.; Yang, Y.; Saleh, L.; Bollinger, J. M.; Solomon, E. I. *J. Am. Chem. Soc.* **2004**, *126*, 3777–3788.

(12) Ghiladi, M.; Gomez, J. T.; Hazell, A.; Kofod, P.; Lumtscher, J.; McKenzie, C. J. *Dalton Trans.* **2003**, 1320–1325.

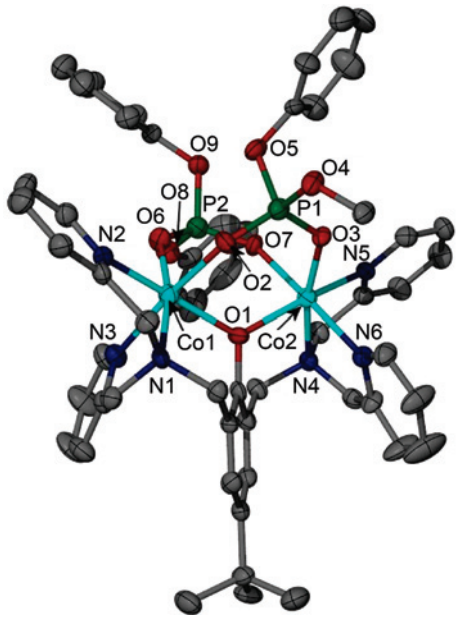

Figure 1. Cation of **1**, showing the atom-labelling scheme (displacement ellipsoids shown at 50% probability). For clarity, H atoms are omitted and only the *ipso* carbon of the phenyl ring bound to O4 is shown. The cations of **2** and **3** display closely comparable gross geometry.

carbon signals are seen, which indicates that **3** must be symmetrical, rendering the C and H atoms in each half of the molecule magnetically identical. The appearance of proton signals in the nonaromatic region corresponding to two protons with geminal coupling substantiates further this assignment. The symmetry is not retained in the crystal structure of **3**.

X-ray Crystal Structures. The structure of the cation in **1** in the solid state is shown in Figure 1. The structures of **2** and **3** are geometrically similar. Two polymorphs of **2** have been observed, both with stoichiometry **2**-$(ClO_4)_2 \cdot C_3H_6O \cdot H_2O$. The geometry of the $Co^{II}Co^{III}$ complex is comparable in the two polymorphic structures. In each of the structures **1**, **2**, and **3**, the connectivities are equivalent and the gross geometries of the complexes are closely comparable. The heptadentate ligand provides four donor atoms to each metal ion: one amine (N1 or N4), two pyridines (N2 and N3 or N5 and N6), and one phenoxide (O1). The remaining two coordination sites are occupied by an O atom from each of the diphenylphosphate groups: O2 and O6 or O3 and O7. The nitrogen donor set on each metal ion coordinates in a facial geometry, and the dimetallic site is triply bridged by the phenoxide O atom of the dinucleating ligand and the two *O*,*O*′-bridging diphenylphosphate groups. Selected crystallographic data and bond lengths and angles for the complexes are given in Tables 1 and 2, respectively. The coordination geometry of Co1 and Co2 for the homovalent complexes **1** and **3** are comparable, while significant bond length and angle variations are evident in the mixed-valence complex **2**. The coordination sphere contraction is apparent for Co^{III} compared to Co^{II}, with the average coordination bond lengths being 1.93 and 2.11 Å for the two ions, respectively. This conformational change can be ascribed to both the change in charge on the metal ion and the spin change between high-spin Co^{II} and low-spin Co^{III}. In general, bond lengths are as expected for Co^{II} and Co^{III} with donor O and N atoms,[13] and the distinct difference in bond lengths for **2** identifies it as a valence-trapped Robin−Day class II complex.[14]

Comparison of the average deviation from 90° for the twelve bite angles where the metal donor atoms are *cis* coordinated (Table 3) shows that the low-spin Co^{III} sites are closer to ideal octahedral geometry than the high-spin Co^{II} sites. The average deviation from 90° bond angles for the two Co^{II} sites in **1** are 5.19° and 5.06°, compared to 5.17/5.15° for the Co^{II} site in **2a/2b**. The distortions for the Co^{III} sites are 2.94/2.71 in **2a/2b**, and 2.89/2.85° for the two sites in **3**, consistent with the preference for octahedral geometry of the low-spin d^6 configuration of Co^{III}. Of the three complexes, the shortest metal−metal separation is 3.5906(17) Å in **3**, despite this complex exhibiting the largest Co1−O1−Co2 angle, 132.2(3)°. Short metal−phenoxide distances (1.972(6) and 1.956(6) Å) counterbalance this factor.

Solid-State NMR Spectroscopy. Paramagnetic shifts give useful information about the local magnetic properties and may be qualitatively predicted by the Goodenough−Kanamori rules.[15,16] It is relatively rare to have access to a series of compounds in which chemically identical phosphate phosphorus atoms are located in three such different local magnetic environments. Delineation of the phosphorus chemical shifts of such a series would give data with predictive capability for the assessment of electronic ground states for other paramagnetic inorganic and organic phosphate systems. Thus, we have measured the solid state ^{31}P magic-angle spinning (MAS) NMR spectra of the diamagnetic $Co^{III}Co^{III}$ (**3**) and the paramagnetic $Co^{II}Co^{III}$ (**2**) and $Co^{II}Co^{II}$ (**1**) complexes (Figure 2).

The solution state ^{31}P NMR spectra of the diamagnetic complex **3** contains a single resonance with $\delta_{iso}(^{31}P) = 2.17$ ppm, which is assigned to the two chemically equivalent phosphorus atoms. In contrast the ^{31}P MAS NMR spectra of a polycrystalline sample of **3** shows two sites with $\delta_{iso}(^{31}P) = -0.7(1)$ and $-15.5(1)$ ppm, respectively, the former signal accounting for about 90% of the spectral intensity (Figure 2c). The two phosphorus atoms are chemically equivalent but not crystallographically equivalent and two sites with a 1:1 intensity ratio might have been expected in ^{31}P solid-state NMR spectra. However, the signals are so different in intensity this cannot be the explanation. Because only one signal is observed by solution NMR spectroscopy, we suggest the minor resonance with $\delta_{iso}(^{31}P) = -15.5(5)$ is due to the presence of a trace of a second polymorph of **3**. The two ^{31}P sites in **3** have similar local coordination environments and therefore observation of almost identical isotropic chemical shifts resulting in overlapping resonances is not surprising. In view of the structural characterization of two polymorphs for **2,** this does not seem unreasonable.

(13) Allen, F. H.; Orpen, A. G.; Taylor, R. *J. Chem. Soc., Dalton Trans.* **1989**, *12*, S1–S83.
(14) Robin, M. B.; Day, P. *Adv. Inorg. Chem. Radiochem.* **1967**, *10*, 247–422.
(15) Goodenough, J. B. *Magnetism and the Chemical Bonding*; John Wiley & Sons: New York, 1963.
(16) Grey, C. P.; Dupre, N. *Chem. Rev.* **2004**, *104* (10), 4493–4512.

Table 1. Crystallographic Data and Experimental Details

	1-$(B(Ph)_4)$	**2**-$(ClO_4)_2 \cdot C_3H_6O \cdot H_2O$[a]	**2**-$(ClO_4)_2 \cdot C_3H_6O \cdot H_2O$[b]	**3**-$(ClO_4)_3 \cdot 3.5H_2O$
empirical formula	$C_{84}H_{79}BCo_2N_6O_9P_2$	$C_{63}H_{67}Cl_2Co_2N_6O_{19}P_2$	$C_{63}H_{67}Cl_2Co_2N_6O_{19}P_2$	$C_{60}H_{66}Cl_3Co_2N_6O_{24.5}P_2$
M_r	1507.14	1462.93	1462.93	1549.34
space group	$P2_1/c$	$P\bar{1}$	$P\bar{1}$	$C2/c$
a [Å]	17.3667(12)	10.1939(4)	10.341(2)	45.883(7)
b [Å]	20.5374(15)	16.6030(7)	13.199(2)	15.370(2)
c [Å]	22.5306(15)	20.0035(8)	24.018(3)	19.544(2)
α [°]	90	84.000(1)	100.199(5)	90
β [°]	112.173(2)	77.223(2)	90.062(5)	91.241(5)
γ [°]	90	83.966(1)	96.831(5)	90
V [Å^3]	7441.6(9)	3271.9(2)	3202.7(9)	13780(3)
Z	4	2	2	8
T [K]	180(2)	180(2)	180(2)	180(2)
ρ_{calcd} [g cm^{-3}]	1.345	1.485	1.517	1.494
μ(Mo Kα) [mm^{-1}]	0.552	0.715	0.730	0.727
$2\theta_{max}$ [°]	44.0	50.0	50.0	44.9
reflns measured	30733	46199	39759	52513
independent reflns	9058	10947	11097	8727
R_{int}	0.086	0.072	0.113	0.128
observed reflns [$I > 2\sigma(I)$]	5075	6627	6024	5264
parameters, restraints	937, 0	809, 0	847, 0	865, 40
$R1$ [$I > 2\sigma(I)$]	0.035	0.059	0.062	0.085
$wR2$ [all data]	0.044	0.168	0.155	0.263
goodness of fit on F^2	0.70	1.04	0.94	1.04
CCDC No.	612974	612975	612976	612977

[a] Polymorph 1 (**2a**). [b] Polymorph 2 (**2b**).

Table 2. Selected Bond Lengths [Å] and Angles [°] for **1**, **2**, and **3**

	1	**2a**	**2b**	**3**
Co1−O1	2.058(2)	2.154(3)	2.158(3)	1.972(6)
Co1−O2	2.136(2)	2.072(3)	2.079(3)	1.901(6)
Co1−O6	2.076(2)	2.068(3)	2.031(3)	1.922(6)
Co1−N1	2.190(2)	2.158(4)	2.163(4)	1.944(7)
Co1−N2	2.131(2)	2.110(4)	2.110(4)	1.915(7)
Co1−N3	2.135(2)	2.115(4)	2.127(4)	1.903(8)
Co2−O1	2.054(2)	1.924(3)	1.939(3)	1.956(6)
Co2−O3	2.040(2)	1.936(3)	1.920(3)	1.921(6)
Co2−O7	2.116(2)	1.935(3)	1.916(3)	1.923(6)
Co2−N4	2.165(2)	1.955(4)	1.951(4)	1.952(7)
Co2−N5	2.133(3)	1.926(4)	1.905(4)	1.899(8)
Co2−N6	2.108(2)	1.940(4)	1.941(4)	1.898(8)
Co1···Co2	3.6648(6)	3.6889(9)	3.7081(11)	3.5906(17)
Co1−O1−Co2	126.1(1)	129.5(2)	129.6(2)	132.2(3)

Table 3. Bite Angles [°] for Metal Donors with cis Geometry

	1	**2a**	**2b**	**3**
O1−Co1−O2	89.25(7)	85.90(12)	86.84(12)	90.3(2)
O1−Co1−O6	98.12(7)	94.96(12)	91.77(12)	93.4(3)
O1−Co1−N1	89.36(8)	90.28(13)	90.50(12)	93.4(3)
O1−Co1−N3	91.54(8)	89.62(13)	91.13(13)	90.7(3)
O2−Co1−O6	90.43(7)	93.61(13)	92.73(12)	89.4(3)
O2−Co1−N1	97.39(8)	93.56(14)	93.78(13)	91.4(3)
O2−Co1−N2	85.11(8)	84.37(14)	84.09(14)	84.7(3)
O6−Co1−N2	96.58(9)	97.27(15)	100.23(14)	91.3(3)
O6−Co1−N3	93.04(9)	92.70(15)	94.09(14)	92.7(3)
N1−Co1−N2	76.88(10)	78.73(15)	78.56(15)	82.0(3)
N1−Co1−N3	79.00(10)	80.49(15)	79.46(15)	86.4(3)
N2−Co1−N3	93.19(9)	98.75(15)	96.47(15)	94.0(3)
Average deviation from 90°[a]	5.06	5.17	5.15	2.89
O1−Co2−O3	98.02(8)	92.42(13)	92.44(13)	91.8(2)
O1−Co2−O7	88.08(7)	89.90(14)	90.61(13)	88.5(3)
O1−Co2−N4	91.52(9)	94.75(15)	94.14(15)	94.2(3)
O1−Co2−N5	90.59(9)	88.68(15)	87.77(14)	93.1(3)
O3−Co2−O7	95.43(8)	91.11(14)	91.31(13)	92.0(3)
O3−Co2−N5	94.17(10)	92.71(15)	91.91(15)	91.9(3)
O3−Co2−N6	94.30(10)	91.45(15)	91.07(15)	92.2(3)
O7−Co2−N4	90.33(8)	90.44(15)	90.48(14)	90.2(3)
O7−Co2−N6	83.04(8)	86.36(15)	87.10(14)	86.5(3)
N4−Co2−N6	77.07(10)	81.50(17)	82.43(16)	82.0(3)
N5−Co2−N4	80.20(10)	85.93(17)	86.50(16)	85.9(3)
N5−Co2−N6	96.25(9)	94.81(17)	94.32(16)	91.7(3)
Average deviation from 90°[a]	5.19	2.94	2.71	2.85

[a] Defined as the mean of the absolute differences between the angle and 90°.

Four isotropic resonances with $\delta(^{31}P) = 2570(40)$, 2870(40), 2990(20), and 3170(40) ppm are identified for **2** by comparing ^{31}P MAS NMR spectra recorded with different spinning speeds (Figure 2b). The observation of four sites confirms the coexistence of **2a** and **2b** in comparable amounts in the solid state. Each phosphorus atom has a single P−O−Co^{II} connectivity. In **2a** these show bond angles of 128.9° and 133.7° and in **2b** the corresponding angles are 132.5° and 131.4°. The size and sign of Fermi-contact shifts are very sensitive to the P−O−Co^{II} bond angles, as, for example, observed for ^{6,7}Li in lithium manganese oxides.[16] Thus, the about 600 ppm variation in ^{31}P isotropic shifts for the four sites is ascribed to these fairly small variations in P−O−Co^{II} bond angles making ^{31}P NMR spectroscopy a strong tool for detecting subtle structural changes.

In **1** each P atom has two P−O−Co^{II} connectivities with bond angles ranging from 127.5 to 137.8°. Thus, because the two Co^{II} are only weakly antiferromagnetically coupled, isotropic shifts twice as large as for **2** are expected. A broad resonance centered at ∼6000 (100) ppm (Figure 2a) can be discriminated, in excellent agreement with the predicted value for the isotropic shifts. Individual peaks for the one or more isotropic resonances cannot be identified because of extremely broad lines caused by the paramagnetism of the sample.

The ^{31}P isotropic shifts ($\delta_{iso}(^{31}P)$) in the series of compounds broaden and shift downfield by about 3000 ppm for each increment in oxidation state. This corroborates the changes in the local magnetic field. Furthermore, ^{31}P solid-state NMR confirms that the bulk samples of each of the compounds are oxidation-state pure. For example, complex **1** contains no signal that would indicate contamination by **2** or **3**.

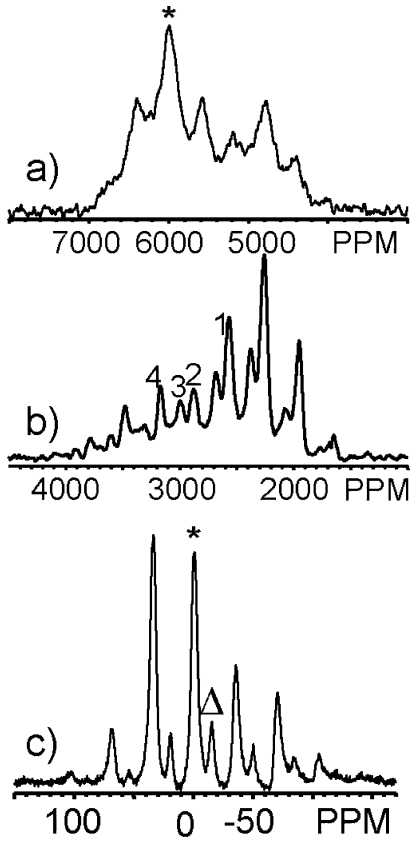

Figure 2. ^{31}P MAS NMR spectra of **1**, **2**, and **3** recorded at 81.29 MHz (υ_r = 33 kHz), 81.06 MHz (υ_r = 25 kHz), and 145.74 MHz (υ_r = 6 kHz), respectively. (a) The spectrum of the weakly antiferromagnetically coupled **1** shows an isotropic resonance for one or more P environments centered around 6000 ppm, as indicated by the asterisk. (b) Paramagnetic **2**: 1, 2, 3, and 4 mark the position of the four isotropic resonances showing that the two polymorphs, **2a** and **2b**, coexist in the solid phase in comparable amounts. (c) The spectrum of diamagnetic **3**. The isotropic resonance is indicated by an asterisk. The isotropic resonance for a second site, tentatively assigned to a second polymorph of **3**, is marked by a triangle (see text).

Electrochemistry. Cyclic voltammetry (CV) and differential pulse voltammetry (DPV) of the three complexes in acetonitrile under dry anaerobic conditions in the potential range −0.69 to 1.63 V (vs $Fc^{0/+}$) are shown in Figure 3, and in the Supporting Information, Figures S1, S2 and S3. Variations in the open circuit potential (OCP) for the three complexes corroborate the assigned oxidation states: **1** [$Co^{II}Co^{II}$] has the lowest OCP of 0.00 V and **3** [$Co^{III}Co^{III}$] has the highest OCP of 0.56 V, while the mixed-valence complex **2** [$Co^{II}Co^{III}$] has an OCP of 0.26 V. Peak potentials are given in Table 4. The cyclic voltammograms are very similar, each showing two anodic ($E_{pa,1}$ and $E_{pa,2}$) and two cathodic ($E_{pc,3}$ and $E_{pc,4}$) peaks, widely separated. Because the $bpbp^-$ and diphenylphosphate ligands are not redox active in the applied potential window, the electrochemical processes must arise from metal-based redox reactions. The anodic peaks are assigned to the sequential one-electron oxidations $Co^{II}Co^{II} \rightarrow Co^{II}Co^{III}$ and $Co^{II}Co^{III} \rightarrow Co^{III}Co^{III}$, while the cathodic peaks are counterpart one-electron reductions. The redox waves are irreversible, suggesting that each oxidation/reduction is followed by a rearrangement, which is both electronic and structural. The Co^{III} ions are low spin while the Co^{II} ions are high spin. Thus, reduction of Co^{III} may initially produce a low-spin Co^{II} species, which presumably undergoes a rapid spin change. These processes will be accompanied by optimization of the Co-ligand bond distances, in accordance with the differences observed in the crystal structures of **1**, **2**, and **3**. Because these geometrical changes do not require any bonds to be broken, the rate of conversion from destabilized to stabilized geometry might well be fast, consistent with the fact that no reversible waves are observed at high scan rates (2 V s^{-1}). The reverse process on the other hand must be slow on the electrochemical time scale because reversible electrochemical behavior is not seen at slow scan rates (0.02 V s^{-1}). An overlay of the measured voltammograms at scan rates from 0.02 to 0.50 V s^{-1} for **1**, **2**, and **3** is shown in the Supporting Information, Figure S1.

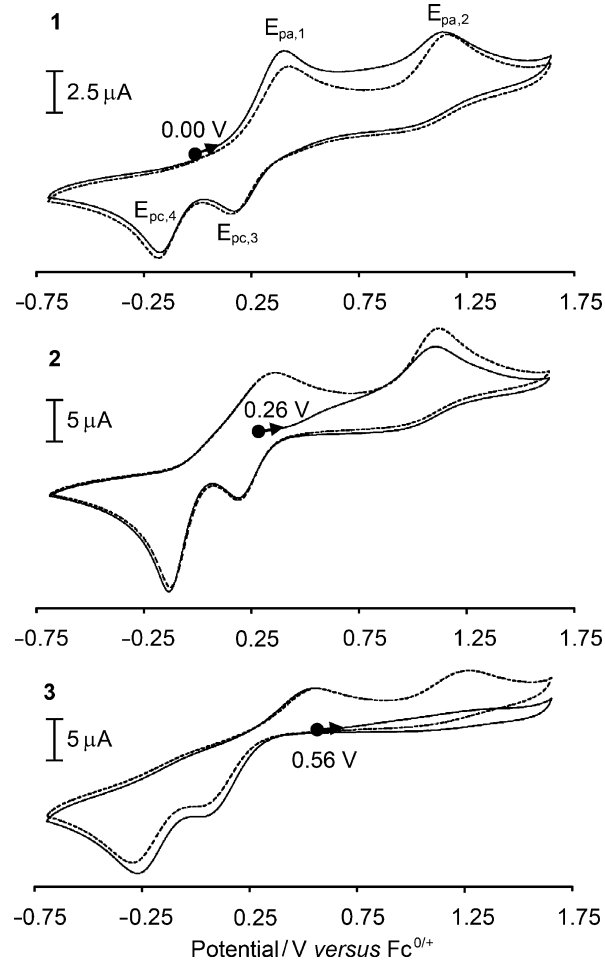

Figure 3. Cyclic voltammograms of **1**, **2**, and **3**, obtained with scan rate 0.20 V s^{-1}. OCP used as start potential, switching potential −0.69 and 1.63 V. The dashed lines indicate the second scan.

Table 4. Peak Potentials (a = anodic, c = cathodic) for **1**, **2**, and **3** Measured by Cyclic Voltammetry (CV) and Differential Pulse Voltammetry (DPV) in Acetonitrile at 25 °C

		CV[a] (DPV[b]) [V]			
complex	OCP	$E_{pa,1}$	$E_{pa,2}$	$E_{pc,3}$	$E_{pc,4}$
1	0.00	0.42 (0.50)	1.18 (1.24)	0.14 (0.05)	−0.19 (−0.36)
2	0.26	0.36 (0.46)	1.13 (1.18)	0.17 (0.02)	−0.15 (−0.32)
3	0.56	0.54 (0.32)	1.24 (1.05)	0.06 (0.13)	−0.29 (−0.19)

[a] Peak potentials at scan rate 0.2 V s^{-1}. [b] Peak potentials at scan rate 0.05 V s^{-1}

Scheme 2. Assignment of the Four Electrochemical Peaks Detected by Voltammetry[a]

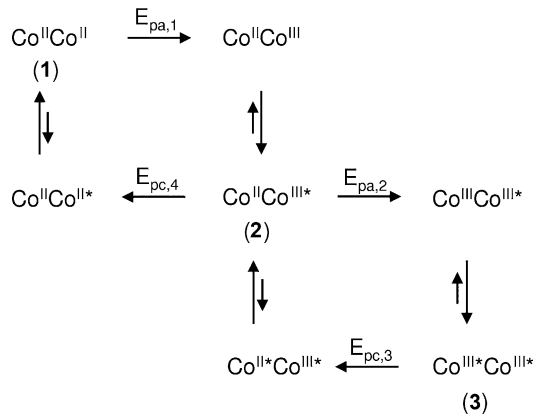

[a] Metal sites with a proposed or verified low-spin electronic configuration are marked with an asterisk.

The electrochemical behavior of **1**, **2**, and **3** is different from that of related iron and manganese complexes, which show reversible or quasi-reversible electrochemistry.[17] We believe this to be a consequence of the induced spin change that occurs when the metal site is oxidized or reduced (i.e., high-spin Co^{II} ↔ low-spin Co^{III}) and the stereochemical inertness of the generated low-spin Co^{III} ion. The first oxidation wave ($E_{pa,1}$) is the one-electron oxidation of **1**, generating a mixed-valence high-spin Co^{II}-high-spin Co^{III} complex which quickly rearranges into the high-spin Co^{II}-low-spin Co^{III} complex **2**. The second oxidation wave then corresponds to one-electron oxidation of **2** to generate a high-spin Co^{III}-low-spin Co^{III} complex which then rearranges into **3**. Similar to the oxidation waves, the reduction wave at $E_{pc,3}$ can be assigned to the one-electron reduction of **3**, which rearranges to **2** and then is reduced at $E_{pc,4}$ to regenerate **1**. These processes are summarized in Scheme 2. The assignments are corroborated by two partial scans on **2** (Supporting Information, Figure S2). Scans between −0.62 and 0.61 V (solid line) show only oxidation of **1** ($E_{pa,1}$) and reduction of **2** ($E_{pc,4}$), while scans between 0.00 and 1.52 V show oxidation of **2** ($E_{pa,2}$) and reduction of **3** ($E_{pc,3}$).

The DPV of **1** and **2** (Supporting Information, Figure S3) gives peak potentials that are almost identical to the potentials measured by CV, while the potentials measured for **3** deviate. This might be due to the high scan-rate dependence of the peak potentials for **3** in the CV measurements (see Supporting Information). The shapes of the DPV diagrams are interesting: the major peaks for **1** are from the two-oxidation processes, while for **3** it is the reduction peaks that give the largest current. The DPV diagram of **2** is almost intermediate between **1** and **3**. Small broad peaks which could correspond to oxidation or reduction of complexes that have not undergone rearrangement are also seen, especially in the DPV of **2** and **3**. The appearance of these small peaks indicates that the geometry rearrangement is not instantaneous.

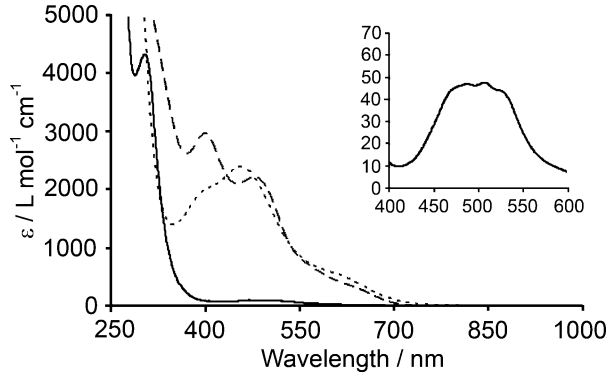

Figure 4. UV−vis spectrum of **1** (solid line), **2** (dotted line), and **3** (dashed line) in acetonitrile at 25 °C. Inset: expanded spectrum of **1** in the 400−600 nm region.

Electronic and Magnetic Properties. UV−visible-NIR data for **1**, **2,** and **3** in CH_3CN are shown in Figure 4, and the data are summarized in Table 5. For **1**, a strong absorption at 303 nm (4300 L mol^{-1} cm^{-1}) is tentatively assigned to a ligand-to-metal charge transfer (LMCT) transition, while the three weak overlapping absorptions at ∼500 nm (insert in Figure 4), are assigned to the $^4T_{1g}\rightarrow{}^4T_{1g}(^4P)$ d−d transition in O_h symmetry, which is split because of the lower symmetry.[18] A broad, weak band at 1094 nm is observed in both **1** and **2** (not shown in Figure 4) which is assignable to the $^4T_{1g}\rightarrow{}^4T_{2g}$ d−d transition in O_h symmetry arising from the Co^{II} ion. Complexes **2** and **3** both show three strong absorption bands in the visible region. The highest energy absorption at 390−400 nm is assigned to a LMCT band from the phenolate to Co^{III}. The two remaining peaks are assigned to the $^1A_{1g}\rightarrow{}^1T_{2g}$ and $^1A_{1g}\rightarrow{}^1T_{1g}$ d−d transitions for octahedral low-spin Co^{III}, the latter having the lowest energy. The transitions are separated by ∼5000−6000 cm^{-1} in both complexes, but the peaks for **3** are red-shifted by ∼1000 cm^{-1} and weaker compared to **2**.

MCD spectra of **1** in a poly(dimethylsiloxane) mull and **2** in ethanol solution are shown in Figure 5, and the data are summarized in Table 5. (While acetonitrile is an excellent solvent for **1**, **2** and **3**, it cannot be used for low temperature MCD because it does not form an optical glass when frozen as does ethanol. Unfortunately, ethanol is a poor solvent for **1**, so the MCD spectra were collected on the mulled solid, which produces higher noise than does an ethanol glass.) All of the peaks are temperature-dependent *C*-terms, indicating that they arise from the high-spin Co^{II} ground state. The spectra show similar peaks in the d−d region, typical of 6-coordinate high-spin Co^{II} species.[19] It is clear from the d−d region that **1** is an all high-spin Co^{II} complex and **2** is a mixed high-spin Co^{II} and low-spin Co^{III} complex. The d−d transitions from Co^{III} that are observed in the absorption

(17) (a) Borovik, A. S.; Que, L, Jr *J. Am. Chem. Soc.* **1988**, *110*, 1986–1988. (b) Borovik, A. S.; Papaefthymiou, V.; Taylar, L. F.; Anderson, O. P.; Que, L, Jr *J. Am. Chem. Soc.* **1989**, *111*, 6183–6195. (c) Albedyhl, S.; Averbuch-Pouchot, M. T.; Belle, C.; Krebs, B.; Pierre, J. L.; Saint-Aman, E.; Torelli, S. *Eur. J. Inorg. Chem.* **2001**, 1457–1464. (d) Ghiladi, M; Jensen, K. B.; Jiang, J.; McKenzie, C. J.; Mø rup, S.; Søtofte, I.; Ulstrup, J. *J. Chem. Soc., Dalton Trans.* **1999**, 2675–2681. (e) Diril, H.; Chang, H.-R.; Nilges, M. J.; Zhang, X.; Potenza, J. A.; Schugar, H. J.; Isied, S. S.; Hendrickson, D. N. *J. Am. Chem. Soc.* **1989**, *111*, 5102–5114.

(18) Das, R.; Nanda, K. K.; Paul, I.; Baitalik, S.; Nag, K. *Polyhedron* **1994**, *13*, 2639–2645.

(19) Kaden, T. A.; Holmquist, B.; Vallee, B. L. *Inorg. Chem.* **1974**, *13*, 2585–2590.

Table 5. UV/Vis/NIR Absorption, MCD, and AOMX Calculations for the Complexes

complex	UV/vis/NIR[a] λ_{max} [nm], ε [$M^{-1}cm^{-1}$]	MCD λ_{max} [nm]	calculated[b]	assignment in O_h symmetry
1[c]	303, 4300			LMCT Co^{II}
		311		trace **2** impurity
		348		phenolateO^- $\rightarrow Co^{II}t_{2g}$
		396		trace **2** impurity
	478, 5	455	479	$^4T_{1g}\rightarrow{}^4T_{1g}(P)$ Co^{II}
	510, 50	503	494	$^4T_{1g}\rightarrow{}^4T_{1g}(P)$ Co^{II}
	522, 45 (sh)	529	530	$^4T_{1g}\rightarrow{}^4T_{1g}(P)$ Co^{II}
	1094, 18		1110	$^4T_{1g}\rightarrow{}^4T_{2g}$ Co^{II}
2[d]	291, 7200 (sh)			LMCT Co^{II} + Co^{III}
	390, 1900 (sh)			LMCT Co^{II} + Co^{III}
	456, 2400			$^1A_{1g}\rightarrow{}^1T_{2g}$ Co^{III}
	615, 500 (sh)			$^1A_{1g}\rightarrow{}^1T_{1g}$ Co^{III}
		311		phenolateO^- $\rightarrow Co^{II}$ e_g
		396		phenolateO^- $\rightarrow Co^{II}$ t_{2g}
		455	469	$^4T_{1g}\rightarrow{}^4T_{1g}(P)$ Co^{II}
		498	495	$^4T_{1g}\rightarrow{}^4T_{1g}(P)$ Co^{II}
		535	532	$^4T_{1g}\rightarrow{}^4T_{1g}(P)$ Co^{II}
	1094, 16		986	$^4T_{1g}\rightarrow{}^4T_{2g}$ Co^{II}
3	329, 4200 (sh)			LMCT Co^{III}
	397, 2950			LMCT Co^{III}
	480, 2200			$^1A_{1g}\rightarrow{}^1T_{2g}$ Co^{III}
	634, 350 (sh)			$^1A_{1g}\rightarrow{}^1T_{1g}$ Co^{III}

[a] In acetonitrile at 25 °C [b] AOMX parameters (cm^{-1}): [c] **1**: $\varepsilon_\sigma(N) = 4500$, $\varepsilon_\sigma(O) = 3170$, ε_σ(phenolateO) = 1790, $B = 770$, ZFS = 122. [d] **2**: $\varepsilon_\sigma(N) = 4230$, $\varepsilon_\sigma(O) = 3980$, ε_σ(phenolateO) = 1790, $B = 681$.

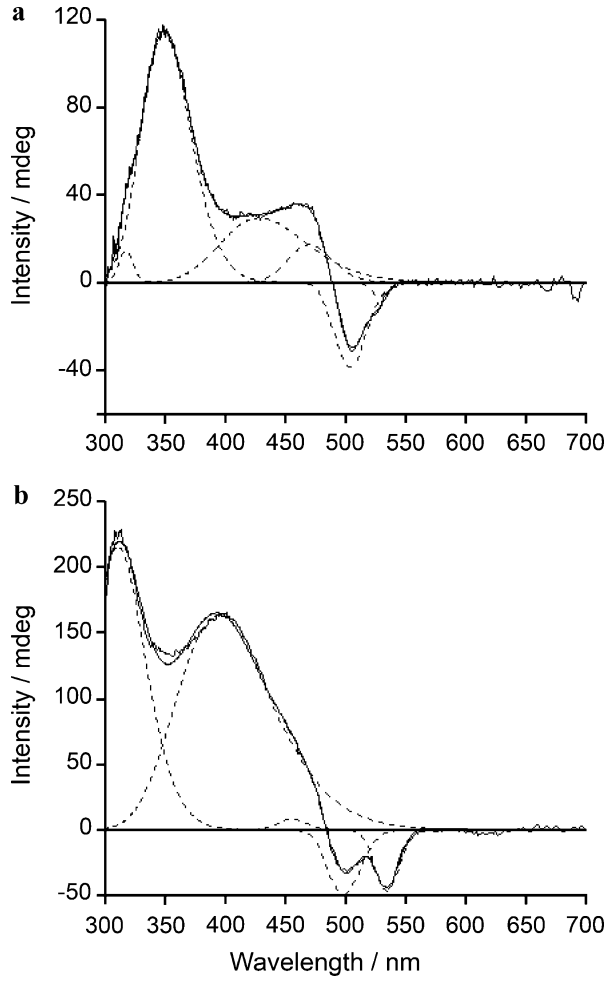

Figure 5. (a) MCD of **1** as a mull in poly(dimethylsiloxane), 10 K, 3.5 T. (b) MCD of **2** in a saturated ethanol solution, 1.6 K, 3.5 T. Spectra were fitted to a minimum number of Gaussian peaks using GRAMS/AI.

spectra are absent from the MCD spectra because a diamagnetic ground-state can only have weak, temperature-independent *A*-terms which are not observed. Differences in the MCD spectra of **1** and **2** are seen in the 300−450 nm region. These are tentatively attributed to charge transfer from phenolate oxygen to Co^{II}. Lever has presented a simplified model for LMCT based on one-electron orbital energies in which octahedral high-spin Co^{II} will have vacancies in both the t_{2g} and e_g levels.[20] Thus, there are four possible LMCT transitions from the phenolate O, namely $\pi\rightarrow t_{2g}$, $\pi\rightarrow e_g$, $\sigma\rightarrow t_{2g}$, and $\sigma\rightarrow e_g$ in order of increasing energy. The two bands at 396 and 311 nm in **2** are assigned to the $\pi\rightarrow t_{2g}$ and $\pi\rightarrow e_g$ LMCT transitions, respectively, and should be separated by $10D_q$. These two bands are separated by ~7000 cm^{-1} which is less than $10D_q$ for Co^{II} with moderate field ligands. This is an approximation because the actual symmetry is lower than O_h and the multiplicity that would be introduced by seven electrons has been ignored. In **1**, only one LMCT is observed at 348 nm, which is presumably the phenolate O $\pi\rightarrow t_{2g}$ LMCT transition. The $\pi\rightarrow e_g$ would be at shorter wavelength than 300 nm and could not be observed since it is hidden beneath more intense electronic transitions from the ligands. It is reasonable that the LMCT transitions to Co^{II} are at higher energies in **1** than in **2** because the $Co^{II}Co^{II}$ dinuclear site should be harder to reduce than the $Co^{II}Co^{III}$ site. A fit of the d−d transitions arising from Co^{II} in **1** and **2** using the angular overlap model (Table 5) demonstrated that the local environment around the metal ions is substantially distorted from O_h symmetry. The bridging phosphate oxygens exert a substantially higher ligand field (ε_σ = 3170 or 3980 cm^{-1}) than the phenolate oxygen (ε_σ = 1790 cm^{-1}). Thus the ligand field symmetry immediately surrounding each Co^{II} is no higher than C_{2v}, which gives a ^4A ground state. The zero-field splitting calculated by the AOM is 122 cm^{-1}.

(20) Lever, A. B. P. *Inorganic Electronic Spectroscopy*; Elsevier: Amsterdam, 1984; p 204.

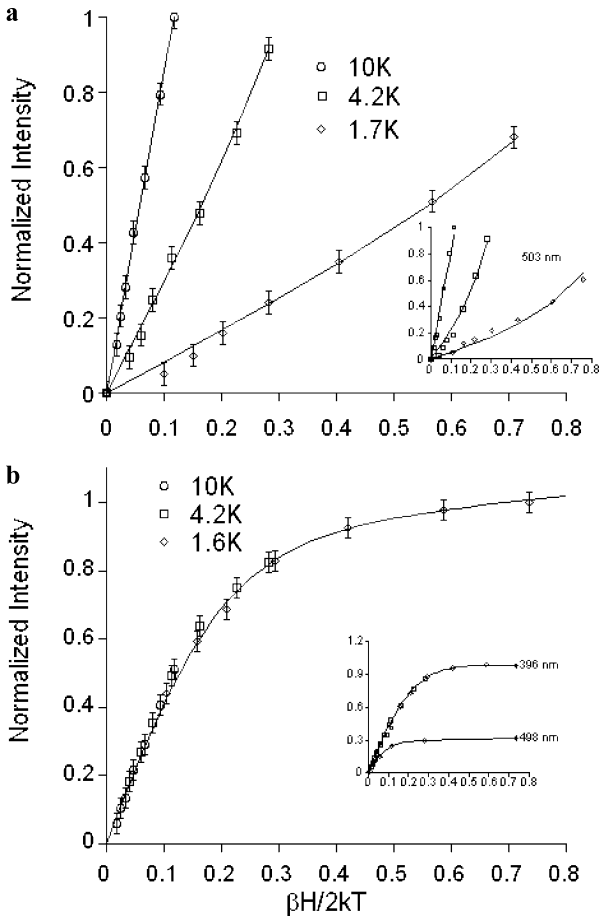

Figure 6. (a) Magnetization plots of the 348 nm MCD band in **1**. The inset shows the magnetization plots for the 503 nm band. The lines through the data represent the best fit to eq 3 with parameters given in Table 6. (b) Magnetization plot of the 311 nm band in **2**. The inset shows the magnetization plots for the 396 and 498 nm bands. The lines through the data represent the best fit to eq 1 with parameters given in Table 6. Only the fits to the 1.6 K data are shown as all temperatures nearly overlay.

Figure 6 shows the magnetization plots for the 348 nm MCD band in **1** and the 311 nm MCD band in **2**. Similar magnetization curves for the 503 nm band are shown in the inset of **1**, and curves for the 396 and 498 nm bands are shown in the inset of **2**. Despite having nearly identical coordination environments, the shapes of the magnetizations plots indicate that the Co^{II} atoms in **1** and **2** have very different ground states. The invariance with wavelength of the shapes of the magnetization curves suggests that all of the MCD transitions in both **1** and **2** are *xy*-polarized.[10a] The temperature-dependent variations in the MCD signal at 348 and 503 nm for **1** indicate weak antiferromagnetic coupling between the two Co^{II} atoms, presumably mediated via the bridging phenolate group. The antiferromagnetic behavior in **1** is made clearer if the MCD intensity is plotted as a function of $1/T$ at a fixed magnetic field, as shown in Figure 7. By contrast, the MCD signals collected at different temperatures for the 311, 396, and 498 nm bands of **2** are nearly superimposed, demonstrating temperature and magnetic field behavior qualitatively similar to a Kramer's doublet with an isotropic *g*-factor for an uncoupled Co^{II} $S = 3/2$ center. Accordingly the orientation-averaged MCD

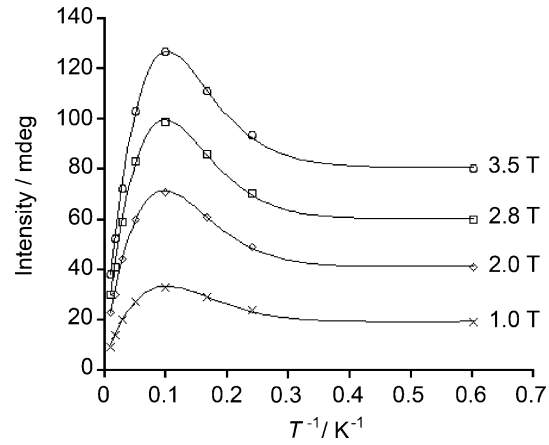

Figure 7. MCD intensity at 348 nm from **1** plotted versus $1/T$ at magnetic fields ranging from 1.0 to 3.5 T. The lines through the data are there as visual guides.

Table 6. Summary of Best Fit Parameters of the VTVH MCD of **1** and **2**

complex **1** (eq 3)	348 nm	503 nm
E_1 [cm^{-1}]	0	0
B_1 [arbitrary]	0.16	0.09
E_2 [cm^{-1}]	7.4	7.4
$I_{satlim2}$ [arbitrary]	15	73
B_2 [arbitrary]	−1.2	−10
δ_2 [cm^{-1}]	<0.1	<0.1
$g_{\|2}$	4.3	4.3
$g_{\perp 2}$	0	0
M_z/M_{xy2}	0	0
E_3 [cm^{-1}]	12.8	12.8
B_3 [arbitrary]	4.7	32

complex **2** (eq 1)	311 nm	396 nm	498 nm
I_{satlim} [arbitrary]	2.3	0.8	0.3
B [arbitrary]	0.01	−0.03	0.01
$g_{\|}$	4.8	4.8	4.8
$g_{\perp}$	4.3	4.3	4.3
M_z/M_{xy}	−0.06	−0.1	−0.1

intensity for an axial doublet at low temperatures and all magnetic fields should be given by Equation 1.[10]

$$\Delta\varepsilon = \mathrm{I_{satlim}}\left[\int_0^{\pi/2} \frac{\cos^2\theta \sin\theta}{\Gamma} g_{\|} \tanh\left(\frac{\Gamma\beta H}{2kT}\right) \mathrm{d}\theta - \sqrt{2}\left(\frac{\mathrm{M}_z}{\mathrm{M}_{xy}}\right)\int_0^{\pi/2} \frac{\sin^3\theta}{\Gamma} g_{\perp} \tanh\left(\frac{\Gamma\beta H}{2kT}\right) \mathrm{d}\theta\right] + \mathrm{BH} \quad (1)$$

I_{satlim} is the *C*-term intensity at saturation, $\Gamma = (g_{\|}^2 \cos^2\theta + g_{\perp}^2 \sin^2\theta)^{1/2}$, β is the Bohr magneton, k is Boltzmann's constant, H is the magnetic field strength, M_z/M_{xy} is the ratio of transition dipole moments of the *z*- and *xy*-polarized transitions, and B is the linear *B*-term intensity. The magnetization plots for **2** (Figure 6b) were fitted to eq 1. The best fit parameters for the 311, 396, and 498 nm bands are given in Table 6, and the solid lines in Figure 6b are the calculated fits of the 1.6 K data using those parameters. The *C*- and *B*-term intensity as well as the polarization should be wavelength dependent since these are determined by the properties of both the excited-state and the ground state. The values of $g_{\|}$ and $g_{\perp}$ depend only on the ground-state and should therefore be independent of wavelength. The small values of M_z/M_{xy} indicate that all bands are *xy*-polarized, which is expected for magnetization that is wavelength independent. The fit to eq 1 is excellent at all wavelengths,

lending assurance that the model used for uncoupled high-spin Co^{II} is appropriate. The MCD magnetization data at different temperatures nearly overlay, and $g_{||}$ and $g_{\perp}$ are nearly equal, indicating that **2** is practically isotropic, despite the low symmetry.

In complex **1**, both metals are high-spin Co^{II} and the unpaired spins on each ion can couple through the phenolate oxygen, with the phosphate pathways providing weaker coupling. The magnitude of the exchange coupling can be determined by analysis of the variable-temperature variable-field (VTVH) MCD intensity (Figure 6a). The theory, equations, and protocols for VTVH MCD data analysis and interpretation in coupled dimers have been worked out and reported over the past twenty years by Solomon and co-workers.[10c,11] The electronic structure of the ground-state of the coupled Co^{II} dimer can be described by the spin Hamiltonian given in eq 2.[10c] This assumes that the ground-state is an effective orbital singlet; an assumption that is validated by the local symmetry around each metal (no higher than C_{2v}), the AOM calculations, and the excellent fit of the magnetic susceptibility data using this spin Hamiltonian (vida infra).

$$\begin{aligned} H = -2JS_1 \cdot S_2 + D_1\left(S_{z1}^2 - \frac{S(S+1)}{3}\right) + R_1(S_{x1}^2 - S_{y1}^2) + D_2 \\ \left(S_{z2}^2 - \frac{S(S+1)}{3}\right) + R_2(S_{x2}^2 - S_{y2}^2) + \\ g_{x1}\beta H_x \cdot S_{x1} + g_{y1}\beta H_y \cdot S_{y1} + g_{z1}\beta H_z \cdot S_{z1} + g_{x2}\beta H_x \cdot S_{x2} + \\ g_{y2}\beta H_y \cdot S_{y2} + g_{z2}\beta H_z \cdot S_{z2} \quad (2) \end{aligned}$$

This Hamiltonian takes into account exchange coupling (J) between the cobalt ions, single-ion axial ($D_{1,2}$) and rhombic ($R_{1,2}$) zero-field splitting parameters and the Zeeman terms ($g_{x1}\beta H_x \cdot S_{x1}$, etc.) for each cobalt ion. The Hamiltonian operates on the uncoupled basis set of wave functions ($|S_1$, M_{s1}, S_2, $M_{s2}|$ where $M_s = 3/2, 1/2, -1/2, -3/2$) that yields a 16×16 matrix. Diagonalization of this matrix in zero magnetic field yields the energies of the dinuclear ground state. The total zero-field splitting, ZFS, is defined here as $\mathrm{ZFS} = |2D[1 + 3(R/D)^2]^{1/2}|$. Equation 2 can be simplified for **1** since the metal ions are symmetrically equivalent ($S_1 = S_2$, $D_1 = D_2$, $R_1 = R_2$, etc.). VTVH MCD data can be directly fit to eq 2, as was recently demonstrated for the coupled ferrous dimer in ribonucleotide reductase by Wei et al.[10c] However, for the analysis of **1** it was more useful to use eq 2 to simulate the 16 energy levels that are required by the fit of the VTVH MCD data to the MCD intensity expression for a series of singlets and doublets given by eq 3 (vida infra). Furthermore, experimentally derived parameters for eq 2 are available from the fit of the magnetic susceptibility data (vida infra). The energy and corresponding M_s for each level using $J = -1.6$ and $D = 44$ cm^{-1} are listed in the Supporting Information, Table S1. It is seen that the manifold of 16 energy levels consists solely of singlets and doublets. This will always be the case as long as the ZFS is nonzero. Furthermore, the only three levels that will be populated at the low temperatures of the MCD experiment are a ground-state singlet, a doublet at $\sim$7 cm^{-1}, and another singlet at $\sim$13 cm^{-1}. All the remaining levels are above 92 cm^{-1}.

The low temperature VTVH MCD data can now be fit to the MCD intensity expression for a series of singlets and doublets for a non-Kramers system (integral spin) to determine the ground-state parameters. This expression is given in eq 3.[10c]

$$\begin{aligned} \Delta\varepsilon = \sum_i \left[(I_{satlim})_i \left(\int_0^{\pi/2} \frac{\cos^2\theta \sin\theta}{\Gamma_i} g_{||i}\beta H \alpha_i \, d\theta - \right.\right. \\ \left.\left. \sqrt{2}\frac{M_z}{M_{xy}} \int_0^{\pi/2} \frac{\sin^3\theta}{\Gamma_i} g_{\perp i}\beta H \alpha_i \, d\theta \right) + B_i H \gamma_i \right] \quad (3) \end{aligned}$$

where

$$\Gamma_i = \sqrt{\delta_i^2 + (g_{||i}\beta H \cos\theta)^2 + (g_{\perp i}\beta H \sin\theta)^2}$$

$$\alpha_i = \frac{e^{-(E_i - \Gamma_i/2)/kT} - e^{-(E_i + \Gamma_i/2)/kT}}{\sum_j e^{-(E_j - \Gamma_j/2)/kT} - e^{-(E_j + \Gamma_j/2)/kT}}$$

$$\gamma_i = \frac{e^{-(E_i - \delta_i/2)/kT} - e^{-(E_i + \delta_i/2)/kT}}{\sum_j e^{-(E_j - \delta_j/2)/kT} - e^{-(E_j + \delta_j/2)/kT}}$$

Equation 3 allows for a linear B-term from field-induced mixing between states. $(I_{satlim})_i$, B_i, δ_i, $g_{||i}$, and $g_{\perp i}$ are the C-term and B-term MCD intensity, the ZFS of the doublet levels, and the dimer g values of the ith doublet, respectively. E_i is the energy of the ith sublevel, and the energy of the ground-state is defined as zero. M_z/M_{xy} is the ratio of transition dipole moments of the z- and xy-polarized transitions. Because the shape of the magnetization curves for **1** are independent of wavelength, the transitions are assumed to be xy-polarized; therefore, initial fits to eq 3 set M_z/M_{xy} and $g_{\perp}$ equal to zero. Furthermore, δ was initially fixed at zero. The VTVH MCD data for **1** was fitted to eq 3 using three energy levels. The best fit at both wavelengths resulted in a ground-state singlet, a doublet at 7.4 cm^{-1} with $g_{||} = 4.3$, and a second singlet at 12.8 cm^{-1}. These energy spacings are consistent with a coupling constant of $J = -1.6$ cm^{-1}. No significant improvements in the fits were obtained when M_z/M_{xy} and $g_{\perp}$ were allowed to float. A small improvement to the fits was observed when δ was allowed to float, but the value for δ was less than 0.1 cm^{-1}. Finally, no significant improvements of the fits of the MCD or magnetic susceptibility data (vida infra) were obtained if a nonzero rhombic ZFS parameter (R in eq 2) was included.

Coupling constants for weak antiferromagnetically coupled Co^{II} dimers have exclusively been determined by magnetic susceptibility (Table 7). Thus confirmation of the VTVH MCD results was in order and accomplished by measurement of magnetic susceptibility on a powder sample of **1** dispersed in Vaseline to prevent a crystallite orientation that can yield anomalous susceptibilities in anisotropic $^4T_{1g}$ (parent state) systems. The maximum at 10 K observed in the $1/T$ plots of the MCD intensity (Figure 7) was confirmed. The maximum in χ_M, per Co^{II}_2, occurs at 9.4 K as shown in Figure 8 and inset. The corresponding $\chi_M T$ values decrease gradually from

Table 7. Summary of Magnetic Coupling in Related Complexes

bridging core	Co···Co [Å]	Co−O−Co [°]	J [cm^{-1}]	reference	CSD refcode
1, $Co_2(\mu\text{-OPhR})(\mu\text{-1,3-}O_2P(OPh)_2)_2$	3.665	126	−1.6	this work	
$Co_2(\mu\text{-OPhR}')(\mu\text{-1,3-}O_2CCH_3)$[a]	3.505	126	−2.7	31	HIMNEW
$Co_2(\mu\text{-OPhR}'')(\mu\text{-1,3-}O_2CCH_3)_2$[b]	3.356	112	−0.22[e,f]	8c	MOYYUU
$Co_2(\mu\text{-OH}_2)(\mu\text{-1,3-}O_2CCH_3)_2$	3.546	113	−0.2[f]	32	ZALXAL
$Co_2(\mu\text{-OH}_2)(\mu\text{-1,3-}O_2CCH_3)_2$	3.687	117	−1.6[f]	7a, c	HUQQOZ
$Co_2(\mu\text{-OPhR})_2$	3.092	97	−6.9[f]	24	GONYOX
$Co_2(\mu\text{-}OG)(\mu\text{-1,3-}O_2CCH_3)$[c]	3.631	127	−1	5b	FIPTEE
$Co_2(\mu\text{-OH}_2)(\mu\text{-1,3-}O_2CCH_3)_2$	3.597	115	−0.7	5a, 6a, 6c	BERWUQ
$Co_2(\mu\text{-}AA)(\mu\text{-1,3-}O_2CCH_3)_2$[d]	3.432	111	−3.6	5a, 6a	UDANIW
$Co_2(\mu\text{-1,3-}O_2CCH_3)_2(\mu\text{-1,1-}O_2CCH_3)$	3.494	108	18.0[e]	5a, 6b	UDANES
MetAP, $Co_2(\mu\text{-OH(H)})(\mu\text{-1,3-}O_2CR)_2$	3.2	98	∼0	2b, 20	

[a] OPhR′ = 2,6-cresolate-N,N,N′,N′-tetramethylene carboxylate. [b] OPhR″ = 2,6-bis[bis(2-hydroxyethyl)aminomethyl]-4-methylphenolate (bhmp$^-$). [c] *OG* = *N*-oxyglutarimide, $C_5H_6NO_3$. [d] *AA* = acetohydroxamate, $CH_3(C{=}O)N(H)\text{-}O^-$. [e] No zero-field-splitting was included in the HDVV model. [f] This model includes an orbital contribution.

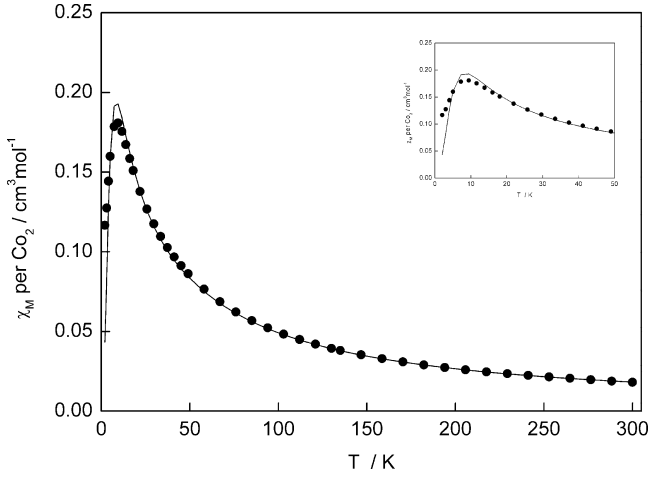

Figure 8. Plot of molar susceptibility, per Co_2, vs temperature (K) for complex **1**. The expanded region of the maximum in χ_M is shown in the inset. The solid line is that calculated using the simplified eq 2 and the parameter values $g = 2.4$, $J = -1.6$ cm^{-1}, and $D = 44$ cm^{-1}.

5.44 cm^3 mol^{-1} K ($\mu_{eff} = 6.59\ \mu_B$), per Co_2, to 4.2 cm^3 mol^{-1} K at ∼50 K, then more rapidly to reach 0.22 cm^3 mol^{-1} K at 2 K. The spin Hamiltonian in eq 2 was simplified according to Bossek et al. to fit susceptibility data.[21]

$$H = -2J\boldsymbol{S}_1\cdot\boldsymbol{S}_2 + \sum_{i=1,2}\{D_i[S_{iz}^2 - S_i(S_i+1)/3] + \mu_B g_i \boldsymbol{S}_i\cdot\boldsymbol{H}\}$$

(simplified eq 2)

A very good fit over the whole 300−2 K temperature range using the simplified Hamiltonian resulted for the parameter set $g = 2.4$, $J = -1.6$ cm^{-1}, $D = 44$ cm^{-1}. The shape of the present $\chi_M T$ plot is similar to those for two triply bridged Co^{II}(tacn) dinuclear species described by Bossek et al.,[21] with $J = -13$ cm^{-1}, $D = 40$ cm^{-1}, but contrasts with the plot found by Ostrovsky et al.[6b] for a triply acetate bridged derivative that showed a maximum in $\chi_M T$ indicative of ferromagnetic coupling ($J = 18$ cm^{-1}). A more complete ligand field/orbital angular momentum model was used in the latter case.[6b] Convergence on coupling parameters that gave good fits to both the magnetic susceptibility data and the MCD data for **1** was an iterative process. The low temperature susceptibility data could also be well fitted using $J = -0.9$ cm^{-1} and $D = -53$ cm^{-1}. However, this results in a doublet at 8.1 cm^{-1} having $M_s = \pm 3$, which is inconsistent with the effective $g \sim 4$ required to fit the MCD data. The VTVH MCD data are very sensitive to g because it governs the steepness of the magnetization curves. So even though the susceptibility data are fitted better with a negative D, a negative D does not produce the correct spin for the lowest doublet. The best fits of the MCD and magnetic susceptibility data are obtained using $J = -1.6$ cm^{-1} and $D = 44$ cm^{-1}. This coupling constant is comparable in sign and magnitude to those reported for related complexes (Table 7). Similar weak antiferromagnetic coupling constants have been determined by temperature-dependent magnetic susceptibility measurements for a number of dinuclear bpbp$^-$ complexes with other metals.[17d] The J's for all but two of the complexes listed in Table 7 were obtained by fitting magnetic susceptibility data to the HDVV model. The good agreement between MCD and magnetic susceptibility in complex **1** strongly suggests that the spin Hamiltonian in eq 2 (the HDVV model) is also appropriate. The only complexes in Table 7 that required a model that included an orbital contribution were $[Co_2(\mu\text{-OPhR}'')(\mu{-}1,3\text{-}O_2CCH_3)_2](BPh_4)$, with J very small and negative,[8c] and $Co_2(\mu{-}1,3\text{-}O_2CCH_3)_2(\mu{-}1,1\text{-}O_2CCH_3)$, and that complex has a relatively large and positive coupling constant of $J = 18$ cm^{-1}.[5a,6b]

The HDVV model assumes that there is no orbital contribution to the exchange interaction because the low-symmetry ligand field removes all orbital degeneracy from the ground state. The model further assumes isotropic exchange between the Co^{II} ions, although single-ion ZFS splitting factors (D and R) and doublet ZFS (δ) were included. This demonstrates that VTVH MCD can be used to measure coupling in weak antiferromagnetic dimers and that the shape of the magnetization curve is very sensitive even to weak coupling. Ostrovsky et al. have demonstrated previously that MCD magnetization is also sensitive to ferromagnetic coupling.[6b] In the ferromagnetic case, the MCD magnetization curves are qualitatively similar to those observed for **2**, but the curves taken at different temperatures are nested rather than overlaid. The MCD of Co^{II} in MetAP has been reported and used to argue that the metals are not antiferromagnetically coupled because the magnetization data from the 6-coordinate Co^{II} can be fitted to a simple doublet

(21) Bossek, U.; Nuhlen, D.; Bill, E.; Glaser, T.; Krebs, C.; Weyhermuller, T.; Wieghardt, K.; Lengen, M.; Trautwein, A. X. *Inorg. Chem.* **1997**, *36*, 2834–2843.

ground-state model, as in **2**, with an isotropic $g = 4.45$.[22] The excellent fits of the MCD and susceptibility data to the HDVV model suggest that orbital contributions are negligible in **1**.[8c,d] This is not always the case for weakly antiferromagnetically coupled dicobalt(II) as has been shown by several groups.[8]

There are too few data on dinuclear Co^{II} complexes to make general statements about the trends in the magnitude of coupling with any certainty, but some speculation is now warranted. First, it is generally assumed that ligands that bridge with a single atom dominate the mediation of magnetic coupling. Second, the nature of the bridging ligand will be important since it affects the strength of the bond between the metal and bridging ligand. Third, in complexes with bridging water, hydroxide, oxide, or phenolate oxygen atoms, in which the principal interaction will be through p-orbitals, the $Co^{II}-O-Co^{II}$ angle is very important because the value of J is the sum of ferromagnetic and antiferromagnetic contributions, which will change with this angle.[23,24] The latter statement may serve to explain why **1** has $J = -1.6\ cm^{-1}$ with a $Co^{II}\cdots Co^{II}$ separation of 3.6648(6) Å and $Co^{II}-O-Co^{II}$ angle of 126.1(1)°, while no coupling was detected in MetAP[22] which has a $Co^{II}\cdots Co^{II}$ separation of only 3.2 Å, but the bridging hydroxide or water has a $Co^{II}-O-Co^{II}$ angle of 98°.[2b]

Conclusion

This study represents the first analysis of a weakly antiferromagnetically coupled $Co^{II}Co^{II}$ system using MCD. The J value so obtained compared well with that obtained from magnetic susceptibility data. A key feature of the study is the synthetic accessibility of the series of complexes. The bis-diphenylphosphate bridged Co_2^{II} system is air stable (in contrast to its carboxylate-bridged counterparts[12,25]) and permits clean generation of the related $Co^{II}Co^{III}$ and Co_2^{III} systems by addition of one equivalent or an excess of a one-electron oxidant. All three complexes can be isolated in the solid state and they retain their oxidation states in solution. This has enabled a structurally analogous $Co^{II}Co^{III}$ system to be used to calibrate the Co_2^{II} result, since coupling is removed in the $Co^{II}Co^{III}$ system, while the spectroscopic properties of the Co^{II} ion remain. A rudimentary correlation of the system described here with the few other dicobalt systems for which data are available suggests that the antiferromagnetic coupling, albeit weak, may be dependent more on the Co−O−Co bridging angle than on the spatial proximity of the two Co^{II} ions. This being the case, the lack of observed antiferromagnetic coupling in MetAP can be explained by its relatively small Co−O−Co bridging angle, despite the relatively short distance between the two Co^{II} ions. Together with a recent study of a ferromagnetic complex,[6b] this study demonstrates that MCD can be used to probe the magnetic properties of dinuclear Co^{II} sites in hydrolase enzymes, providing a valuable alternative for systems which may not lend themselves to magnetic susceptibility studies.

Experimental Section

Elemental analyses were performed at the Chemistry Department II at Copenhagen University, Denmark and Atlantic Microlab, Inc., Norcross, Georgia 30091, U.S.A. UV/vis spectra were recorded on a Shimadzu UV-3100 spectrophotometer. Electrospray Ionization Mass Spectra (ESI MS) were obtained using a Finnigan TSQ 700 triple quadrupole instrument equipped with a Finnigan API source in the nanoelectrospray mode. $^{13}C\{^1H\}$- and ^1H NMR were measured on a Varian Gemini 300 spectrometer at 298 K. Chemical shifts were referenced to the residual signals of the deuterated solvent CD_3CN and are reported versus $SiMe_4$. 2,6-Bis[(bis-(2-pyridylmethyl)amino)methyl]-4-tertbutylphenol (bpbpH) was prepared as described previously.[26]

Synthetic procedure. ***Caution!*** *Although no problems were encountered in the preparation of the perchlorate salts, suitable care should be taken when handling such potentially hazardous compounds.*

[(bpbp)Co_2(O_2P(OPh)$_2$)$_2$](ClO_4)·H_2O, 1-(ClO_4)·H_2O. Hbpbp (0.8786 g, 1.53 mmol) and $Co(ClO_4)_2\cdot 6H_2O$ (1.1225 g, 3.08 mmol) were dissolved in 15 mL of hot CH_3CN to give a maroon solution, to which $HPO_2(OPh)_2$ (0.7692 g, 3.08 mmol) dissolved in 6 mL of CH_3CN was added. Pink needles formed as the solution cooled. The solution was left in the refrigerator overnight and the product was then isolated and washed with a small amount of cold CH_3CN. Yield first crop, 1.1050 g. The mother liquor was concentrated to ~10 mL and 1/2 mL of 2.5 M NaOH was added to give a second crop. Yield second crop: 0.5631 g. The combined products were recrystallized by slow evaporation of an acetonitrile solution (~100 mL) containing 0.60 g of $NaClO_4\cdot H_2O$. Yield 1.3900 g (69%). Elemental analysis calcd (%) for **1**-(ClO_4)·H_2O, $C_{60}H_{61}ClCo_2N_6O_{14}P_2$: C 55.20, H 4.71, N 6.44; found: C 54.85, H 4.29, N, 6.12. ESI MS (CH_3CN): *m*/*z* 1187.9 ([(bpbp)Co_2(O_2P(OPh)$_2$)$_2$]$^+$, 100%). Block-shaped pink crystals of **1**-($B(Ph)_4$) suitable for single crystal X-ray analysis were obtained by exchange of the perchlorate counteranion for the tetraphenylborate counteranion, by slow diffusion of toluene into a mixture of a CH_2Cl_2 solution of **1**-(ClO_4) with 1.5 equiv of $NaBPh_4$ dissolved in acetone.

[(bpbp)Co_2(O_2P(OPh)$_2$)$_2$](ClO_4)$_2$·C_3H_6O·H_2O, 2-(ClO_4)$_2$·C_3H_6O·H_2O. $(NH_4)_2[Ce(NO_3)_6]$ (0.2206 g, 0.40 mmol) was added to a solution of **1**-(ClO_4) (0.4728 g, 0.37 mmol) dissolved in 10 mL of DMF to give a dark brown solution. $NaClO_4\cdot H_2O$ (0.2700 g, 1.90 mmol) dissolved in 2 mL of DMF was added and the product was precipitated as a dark brown powder by addition of 40 mL of H_2O. The powder was recrystallized from acetone/water, providing brown crystals of **2a** and **2b** suitable for single crystal X-ray analysis. Yield 0.3795 g (70%). Elemental analysis calcd (%) for **2**-(ClO_4)$_2$·C_3H_6O·H_2O, $C_{63}H_{67}Cl_2Co_2N_6O_{19}P_2$: C 51.72, H 4.62, N 5.74; found: C 51.82, H 3.89, N 5.93. ESI MS (CH_3CN): *m*/*z* 593.9 ([(bpbp)Co_2(O_2P(OPh)$_2$)$_2$]$^{2+}$, 100%)

[(bpbp)Co_2(O_2P(OPh)$_2$)$_2$](ClO_4)$_3$·3.5 H_2O, 3-(ClO_4)$_3$·3.5H_2O. $(NH_4)_2[Ce(NO_3)_6]$ (2.2206 g, 4.02 mmol) was added to **1**-(ClO_4) (0.4990 g, 0.39 mmol) dissolved in 10 mL of DMF to give a very

(22) Larrabee, J. A.; Leung, C-H.; Moore, R. L.; Thamrong-nawasawat, T.; Wessler, B. S. H. *J. Am. Chem. Soc.* **2004**, *126*, 12316–12324.
(23) Hotzelmann, R.; Wieghardt, K.; Florke, U.; Haupt, H-J.; Weatherburn, D. C.; Bonvoisin, J.; Blondin, G.; Girerd, J.-J. *J. Am. Chem. Soc.* **1992**, *114*, 1681–1696.
(24) Black, D.; Blake, A. J.; Dancey, K. P.; Harrison, A.; McPartlin, M.; Parsons, S.; Tasker, P. A.; Whittaker, G.; Schroder, M. *J. Chem. Soc., Dalton Trans.* **1998**, 3953–3960.
(25) Wackerbarth, H.; Larsen, F. B.; Glaargaard Hansen, A.; McKenzie, C. J.; Ulstrup, J. *Dalton Trans.* **2006**, 3438–3444.
(26) Ghiladi, M.; McKenzie, C. J.; Meier, A.; Powell, A. K.; Ulstrup, J.; Wocaldo, S. *J. Chem. Soc., Dalton Trans.* **1997**, 4011–4018.

dark brown solution. $NaClO_4 \cdot H_2O$ (0.4670 g, 3.34 mmol) dissolved in 3 mL of DMF was added and the product was precipitated by addition of 70 mL of H_2O. The powder was recrystallized from acetone/water to yield red needles suitable for single crystal X-ray analysis. Yield 0.3211 g (53%). Elemental analysis calcd (%) for **3**-$(ClO_4)_3 \cdot 3.5H_2O$, $C_{60}H_{61}Cl_3Co_2N_6O_{22}P_2$: C 47.90, H 4.09, N 5.59; found: C 47.81, H 3.78, N 5.32. ESI MS (CH_3CN): *m*/*z* 643.4 ($[(bpbp)Co_2(O_2P(OPh)_2)_2(ClO_4)]^{2+}$, 100%). NMR $\delta_C\{^1H\}$ (75 MHz; CD_3CN) 31.19 (3 C, s, $C(CH_3)_3$), 35.33 (1 C, s, $C(CH_3)_3$), 40.15 (2 C, s), 68.31 (2 C, s), 68.56 (2 C, s), 120.25 (4 C, d, *J* 5.5, P−O−C−*C*), 120.40 (4 C, d, *J* 5.8, P−O−C−*C*), 122.21 (2 C, s), 125.76 (2 C, s), 126.51 (2 C, s), 127.12 (4 C, s), 127.17 (4 C, s), 127.50 (2 C, s), 127.66 (2 C, s), 130.82 (2 C, s), 131.10 (2 C, s), 131.83 (2 C, s), 142.97 (2 C, s), 143.78 (2 C, s), 149.26 (1 C, s), 150.75 (2 C, s), 151.23 (2 C, d, *J* 7.5, P−O−*C*), 151.71 (2 C, d, *J* 7.4, P−O−*C*), 153.52 (2 C, s), 154.59 (1 C, s), 163.59 (2 C, s), 165.44 (2 C, s). δ_H (300 MHz; CD_3CN) 1.19 (9 H, s, $C(CH_3)_3$), 3.18 (2 H, d, *J* 13), 3.95 (2 H, d, *J* 16), 4.03 (2 H, s), 4.06 (2 H, s), 4.10 (2 H, d, *J* 13), 4.89 (2 H, d, *J* 16), 6.72 (2 H, d, *J* 7.3), 6.79−6.83 (4 H, m), 7.05−7.07 (6 H, m), 7.14 (2 H, s), 7.35−7.44 (8 H, m), 7.48−7.58 (6 H, m), 7.62−7.68 (4 H, m), 8.12 (2 H, dd, *J* 7.8 and 1.2), 8.16 (2 H, d, *J* 5.4), 8.55 (2 H, d, *J* 5.5).

X-ray Crystallography. Analyses of **1**-$(B(Ph)_4)$, **2**-$(ClO_4)_2 \cdot C_3H_6O \cdot H_2O$ (two polymorphs), and **3**-$(ClO_4)_3 \cdot 3.5\ H_2O$ were performed at 180(2) K using a Bruker Nonius X8-APEXII instrument. Crystallographic data and refinement details are given in Table 1. All structures were solved by direct methods and refined against all F^2 data using *SHELXTL* ver. 6.10.[27] All H atoms bound to C atoms were placed in calculated positions and refined using a riding model. Unless otherwise stated below, all non-H atoms were refined with anisotropic displacement parameters. Crystals of **1**-$(B(Ph)_4)$ were weakly diffracting, and data were truncated to 0.95 Å resolution, with about 50% of data observed at the $2\sigma(I)$ level to that resolution. For one polymorph of **2**-$(ClO_4)_2 \cdot C_3H_6O \cdot H_2O$ (**2a**), one phenyl ring belonging to one diphenyl phosphate group was modeled as disordered over two orientations (site occupancy factors 0.75:0.25), related by rotation about the P−O bond. The geometries of these two rings were constrained to be regular hexagons, and the atoms were refined with isotropic displacement parameters. The other phenyl ring of the same diphenyl phosphate group has significantly distorted anisotropic displacement parameters, suggesting some degree of disorder that corresponds to dynamic/static disorder in the plane of the phenyl ring, which was not modeled explicitly. For **3**-$(ClO_4)_3 \cdot 3.5H_2O$, one perchlorate anion and all solvent molecules were poorly resolved and some voids remain in the structure, indicating the likely presence of more diffuse solvent. Application of a continuous solvent-area model[28] with the disordered perchlorate and all water molecules omitted gave significant improvements to the *R* values ($R1 = 0.068$, $wR2 = 0.181$) and suggested up to 8 molecules of water per formula unit. The empirical formula is therefore an approximation. Elemental analysis of **3** gave the best agreement by including only one water solvent molecule in the formula, suggesting that the lattice solvent evaporates during vacuum drying of the product.

Solid-State NMR Spectroscopy. ^{31}P MAS NMR spectra of polycrystalline samples were recorded at 4.7 T (80.86−81.3 MHz) for **1** and **2** using a 2 mm MAS probe. These were recorded using a Hahn echo sequence to alleviate spectrometer dead time and probe ringing and 25−35 kHz spinning. Spectra were recorded with carrier frequencies ranging from 80.86 to 81.4 MHz to cover the entire chemical shift range for the two compounds. For **3**, which is diamagnetic, a field of 8.1 T (145.7 MHz) and 5−8 kHz spinning was employed. All spectra are referenced to neat 85% H_3PO_4 ($\delta_{iso} = 0$ ppm).

Electrochemistry. Cyclic Voltammetry (CV) and Differential Pulse Voltammetry (DPV) were recorded in acetonitrile solution under dry anaerobic conditions using an Autolab system (Eco Chemie, The Netherlands), controlled by the GPES software. The working electrode was a platinum disk, auxiliary electrode a platinum wire, and reference electrode Ag/Ag^+ (0.01 M $AgNO_3$). 0.1 M $TBAClO_4$ (TBA = tertbutylammonium) was used as electrolyte, and all potentials are given versus the ferrocene/ferrocenium ($Fc^{0/+}$) redox couple ($E_{1/2} = 88$ mV vs Ag/Ag^+, $\Delta E = 75-80$ mV). Concentrations of the sample solutions were 1.3 mM for **1**, 2.3 mM for **2**, and 2.2 mM for **3**.

Magnetic Susceptibilities. Variable temperature magnetic susceptibilities on complex **1** were obtained using a Quantum Design MPMS5 Squid magnetometer in a DC field of 1 T. To eliminate any crystallite "torquing" at low temperatures, because of anisotropy in χ_M for high-spin Co(II) ($^4T_{1g}$) species, the ~20 mg sample was dispersed in Vaseline and the χ_M value at 300 K was set at the value using an accurately weighed powder sample.

Spectroscopy. Absorption spectra were recorded on a Cary 6000i UV/visible/near-infrared absorption spectrometer. MCD spectra were recorded at 2 nm bandwidth on a JASCO J-600 spectropolarimeter equipped with an Oxford SM-4 magnetic/cryostat with an Oxford ITC-4 temperature controller. Temperatures were measured with a Lake Shore Cryogenics carbon/glass resistor calibrated between 1.45 and 99.99 K and located 2 mm from the sample. Complex **2** was dissolved in ethanol, which forms an optically clear glass when frozen, and placed in a 0.62 cm pathlength brass cell with quartz windows. Complex **1** was run as a mull in poly(dimethysiloxane) because it was not sufficiently soluble in ethanol. The zero-field spectrum was subtracted as a blank. Details of the MCD data collection have been previously published.[29] MCD spectra were fitted to the minimum number of Gaussian peaks using the GRAMS/AI software (Thermo Electron Corporation).

Angular overlap model (AOM) calculations were made using AOMX, a program based on routines developed by Hoggard for d^3 transition metal ions and extended to d^n systems by Adamsky.[30] AOMX determines the optimum ligand-field parameters needed to fit an observed set of d−d transitions based on a given structure. The two cobalt ions were treated separately. Input to AOMX requires the ligand coordinates (polar r, θ, φ or Cartesian x, y, z) referred to the metal ion at the origin. The cobalt ligand set was assumed to be 3 equivalent nitrogens, 2 equivalent oxygens from the bridging phosphate groups, and the unique phenylate bridging oxygen. AOMX does not use the bond distances to fit the spectrum,

(27) Sheldrick, G. M. *SHELXTL*; Bruker AXS: Madison, WI, 2000.
(28) (a) van der Sluis, P.; Spek, A. L. *Acta Crystallogr.* **1990**, *A46*, 194–201. (b) Spek A. L. *SQUEEZE, implemented in PLATON, A Multipurpose Crystallographic Tool*; Utrecht University: Utrecht, The Netherlands, 1998.
(29) Larrabee, J. A.; Alessi, C. M.; Asiedu, E. T.; Cook, J. O.; Hoerning, K. R.; Klingler, L. J.; Okin, G. S.; Santee, S. S.; Volkert, T. L. *J. Am. Chem. Soc.* **1997**, *119*, 4182–4196.
(30) Hoggard, P. E. In *Topics in Current Chemistry*; Springer-Verlag: Berlin, 1994; Vol. *171*, pp 113−141. The AOMX program is maintained by H. Adamsky, Institut fur Theoretische Chemie, Heinrich Heine Universitat, Duesseldorf, Germany; E-mail: adamsky@theochem.uni-duesseldorfde. The program can also be run on the web using the AOMX server at http://www.theochem.uni-duesseldorf.de/users/heribert/aomx/start.main.html.
(31) Cai, L.; Xie, W.; Mahmoud, H.; Han, Y.; Wink, D. J.; Li, S.; O'Connor, C. J. *Inorg. Chim. Acta* **1997**, *263*, 231–245.
(32) Coucouvanis, D.; Reynolds, R. A.; Dunham, W. R. *J. Am. Chem. Soc.* **1995**, *117*, 7570–7571.

only the bond angles are important, and these are fixed by the crystal structure. However, the bond distances are reflected by the magnitude of the resulting ligand field parameters, ε_σ and ε_π.[30]

Acknowledgment. C.J.M. is grateful to the Danish Natural Science Research Council. J.A.L. acknowledges the National Science Foundation of the U.S.A. (Grant CHE-0554083) for financial support, Professor Edward I. Solomon, Stanford University, for providing the MCD fitting programs, and Professor Natasa Mitic, University of Queensland for assistance in setting up the MCD fitting programs. U.G.N. acknowledges the Danish Science Foundation for a Steno Fellowship (Grant 272-06-0058) and Professor Clare P. Grey, Stony Brook University, for generous access to NMR instruments. K.S.M. acknowledges support from the Australian Research Council for the magnetic work and the Villum Kann Rasmussen (Velux) Foundation, Denmark, and the Department of Physics and Chemistry, University of Southern Denmark, for a Fellowship (May-June 2007) that enabled this work to be finalized and discussed.

Supporting Information Available: Figures S1−S3, cyclic voltammetry; Figure S4, energy level diagrams; Table S1, energy levels (PDF). This material is available free of charge via the Internet at http://pubs.acs.org.

IC7020534